AIAA Atmospheric and Space Environments Conference
2 – 5 August 2010, Toronto, Ontario, Canada

AIAA 2010-7992

Wake-Vortex Topology, Circulation, and Turbulent Exchange Processes

Frank Holzäpfel[1], Takashi Misaka, and Ingo Hennemann
Institut für Physik der Atmosphäre, Deutsches Zentrum für Luft- und Raumfahrt
82234 Oberpfaffenhofen, Germany

Large eddy simulations of aircraft wake vortex evolution in various turbulent and stably stratified atmospheric environments have been conducted with two different LES codes. Passive tracers are used to investigate exchange processes between the vortex cores, the vortex oval and its environment as well as redistribution processes along the vortex tubes. A post processing method is employed to identify the vortex center lines even in progressed states of vortex decay where the coherent vortex structure is getting lost. This method allows, for example, analyzing the circulation evolution of vortex rings, establishing statistics of vortex deformation, and revealing the mechanisms of the vortex bursting phenomenon. Vortex bursting is related to the collision of secondary vorticity structures propagating along the vortex lines. In neutrally and weakly stratified environments long-living vortex rings are observed where circulation decay proceeds in three phases. During the initial diffusion phase vortex decay may depend on integral turbulence length scales. On average, the detrainment of a passive tracer from the primary vortices is correlated with circulation decay.

I. Introduction

THE comprehensive and detailed understanding of wake vortex behavior is crucial for the development of wake vortex systems that aim at increasing the awareness of wake vortex risks or tend to increase airport capacity. The first part of this paper focuses on aspects of the development of vortex topology and circulation decay that may both be relevant for the severity of potential vortex encounters. Another topic is the turbulent mixing and detrainment of the ice crystals generated from the exhaust jets. Their dispersion during the vortex descent is an important parameter in order to quantify the vertical extent, optical thickness, and lifetime of the contrails produced during cruise. Currently, it is not yet clear how strong the contribution of contrails to global warming might be[17].

It turns out that both topics are complementary allowing an improved understanding of wake vortex physics. In particular, two issues raised by Spalart[15] in his Annual Review of Fluid Mechanics are picked up: (i) the controversial concepts of "predictable decay" and "stochastic collapse." Here it is found that depending on the environmental conditions circulation decay characteristics may either feature two-phase or three-phase behavior or continuous decay. (ii) The mechanisms leading to the vortex bursting phenomenon. Here the analysis indicates that collisions of secondary vorticity structures propagating along the vortex lines lead to local spreading of tracers which, however, is not connected to local vortex decay.

From lidar observations it is known that wake vortices may frequently live much longer than anticipated by the aircraft separations that have to be obeyed during approach and landing or during departures. One reason why the procedures are safe nevertheless certainly is related to the transport of the vortices away from the flight corridor by crosswind and vortex descent. Another potential reason is the fact that the vortices do not remain straight but are rapidly deformed by the relatively strong turbulence prevailing in the atmospheric boundary layer. The deformation of vortex segments may reduce the impact time of adverse forces and moments experienced by an encountering aircraft and thus may alleviate the severity of the encounter.

In order to establish statistics of vortex deformation in terms of curvature radii a post processing method is employed to identify the vortex center lines even in progressed states of vortex decay where the coherent vortex structure is getting lost. Moreover, this method allows investigating circulation decay characteristics depending on eddy dissipation rate, integral turbulence length scales, and temperature stratification in greater detail.

[1] Research Scientist, frank.holzaepfel@dlr.de

Copyright © 2010 by the American Institute of Aeronautics and Astronautics, Inc. All rights reserved.

Further, the turbulent exchange processes between the descending vortex oval and its environment are investigated. For this purpose we track the mixing and detrainment of a passive tracer for various initial tracer distributions within the vortex pair and for different environmental conditions. The sometimes contradictory visible tracer footprints and the underlying vortex dynamics are reconciled for the phenomena of pressure waves visualized by helical instabilities and of vortex bursting frequently also termed puffs or pancake vortices.

II. Numerical Methods and Initial Conditions

We have conducted Large Eddy Simulations (LES) of wake vortex evolution in environments with various degrees of atmospheric turbulence and stable temperature stratification employing two different LES codes. The numerical features of the first LES code LESTUF are described in detail in Ref. 1. LESTUF solves the Boussinesq-approximated Navier-Stokes equations in staggered and Cartesian coordinates with a finite differences method of second order accuracy (central finite differences in space and Adams-Bashforth scheme in time). A modification of the Smagorinsky subgrid scale closure[2] reduces wake vortex core growth rates.

The second LES code MGLET[3] also solves the Boussinesq-approximated Navier-Stokes equations discretized by a finite-volume zonal-grid method with non-equidistant staggered variable arrangement. A fourth-order compact scheme is used for the implicit spatial interpolation and differentiation of variables by solving a tri-diagonal system which can achieve spectral-like resolution[4]. The third-order Runge-Kutta method is used for time integration. The pressure field is calculated iteratively employing the HSMAC (Highly Simplified Marker-And-Cell) method in order to reduce the divergence of the velocity field below a prescribed threshold value. Equations for passive scalars have been implemented for investigations of turbulent mixing. Parallel computation is realized by a domain decomposition approach. The Lagrangian dynamic subgrid scale model[5] accounts for reduced turbulent mixing in the centrifugally stable vortex core regions.

Domain sizes of $L_x \times L_y \times L_z = 400 \times 256 \times 256$ m^3 have been applied for LESTUF and of $L_x \times L_y \times L_z = 400 \times 384 \times 512$ m^3 for MGLET with a uniform grid of 1 m, where x denotes flight direction, y spanwise direction, and z vertical direction. Periodic boundaries are employed in all directions. The trailing vortices of an A340-300 aircraft are represented by two counter-rotating Lamb-Oseen vortices with a vortex separation of $b_0 = 47.1$ m and a vortex core radius of $r_c = 3$ m. LESTUF simulates an aircraft during approach with an initial root circulation of $\Gamma_0 = 458$ m²/s whereas MGLET employs a slightly higher value of $\Gamma_0 = 530$ m²/s to represent cruise conditions. In order to account for jet and boundary layer turbulence entrained into the vortices during vortex roll-up an additional rms velocity with a maximum of 2 m/s is added in the vortex core radius vicinity.

The employed combinations of environmental parameters are listed in table 1. The intensity of atmospheric turbulence is expressed in terms of normalized eddy dissipation rates $\varepsilon^* = (\varepsilon\, b_0)^{1/3}/w_0$ and the degree of stable temperature stratification in terms of normalized Brunt-Väisälä frequencies $N^* = t_0 (g/\theta_0\, d\theta/dz)^{1/2}$. In these equations $w_0 = \Gamma_0/(2\pi\, b_0)$ corresponds to the initial wake vortex descent speed, $t_0 = 2\pi\, b_0^2/\Gamma_0$ to the time scale of the vortex pair, and θ to the potential temperature of the atmosphere. Prior to the inset of the counter-rotating vortex pair, the atmospheric turbulence in the differently stratified environments was allowed to develop from prescribed spectral distributions to a state with a distinct inertial subrange and a constant eddy dissipation rate. A series of LESTUF simulations with varying integral turbulence scales, L_t, at $\varepsilon^* = 0.23$, $\boldsymbol{N}^* = 0$ complements the cases listed in table 1.

The analysis of in-situ measurements of the Falcon research aircraft[6] at altitudes between 9 and 11 km indicates Brunt-Väisälä frequencies typically ranging from 0.011 s^{-1} to 0.023 s^{-1} and dissipation rates between 10^{-8} m^2/s^3 and $2\cdot10^{-7}$ m^2/s^3. For the MGLET simulations we employ $\boldsymbol{N}^* = 0.35$ (0.013 s^{-1}) and $\varepsilon^* = 0.01$ ($1.2\cdot10^{-7}$ m^2/s^3) as a typical reference case for cruise conditions. This reference case is complemented by adjacent atmospheric conditions of enhanced or reduced turbulence and stratification, respectively.

ε^* \ N^*	0	0.35	1.0
0		M	
0.01	L/M	L/**M**	L/M
0.05	L	L/M	L
0.23	L	L	L

Table 1. Environmental conditions simulated with LESTUF (L) and MGLET (M).

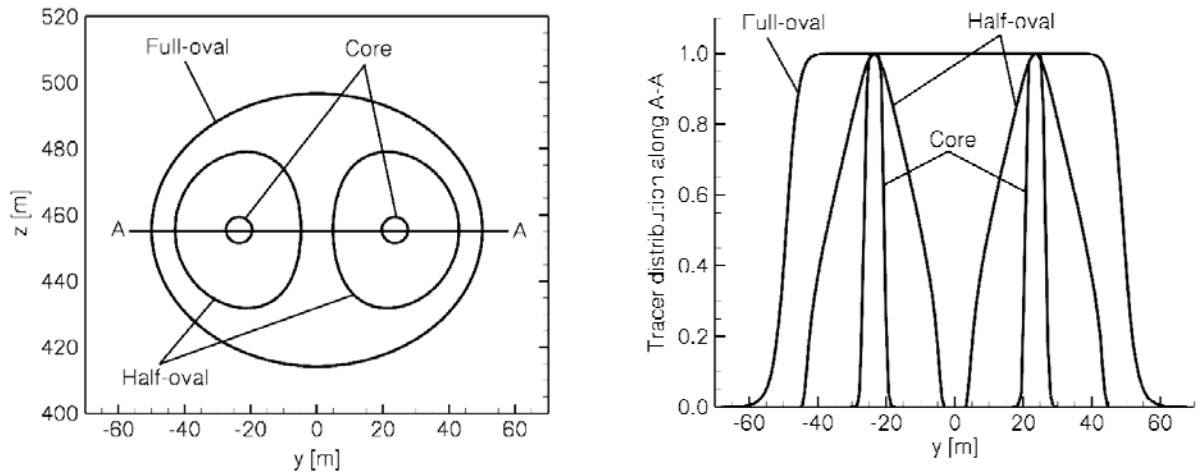

Figure 1. Sketch indicating the initial distributions of passive tracers for three different cases (MGLET).

In order to investigate turbulent mixing processes, MGLET solves equations for two different passive tracers in the left and right vortex. Figure 1 sketches the employed three different initializations: two rather academic cases where the tracers are either trapped in the vortex cores or in the vortex oval and a more realistic case derived from photographs of contrails. Here the tracers are confined within streamlines such that half of the vortex oval is covered by the tracers.

III. Circulation Decay Characteristics

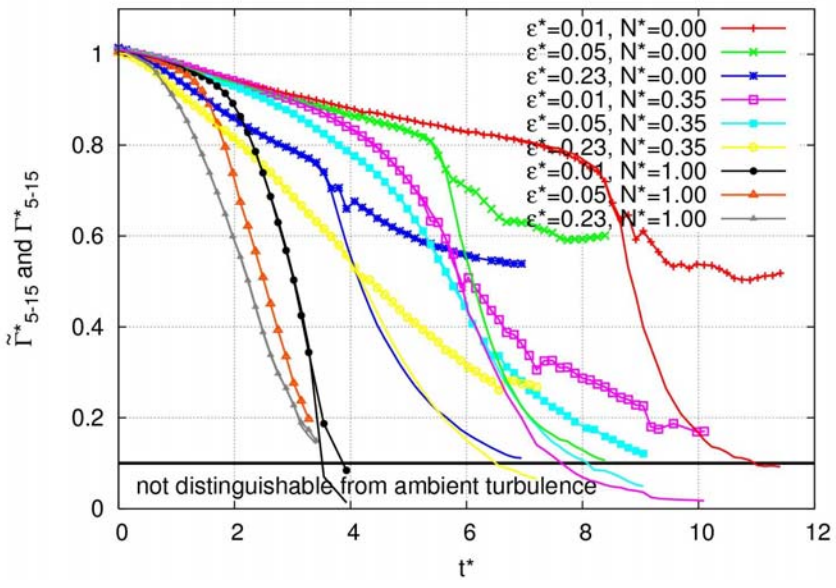

Figure 2. Circulation evolutions of LESTUF simulations for different degrees of ambient turbulence and temperature stratification.

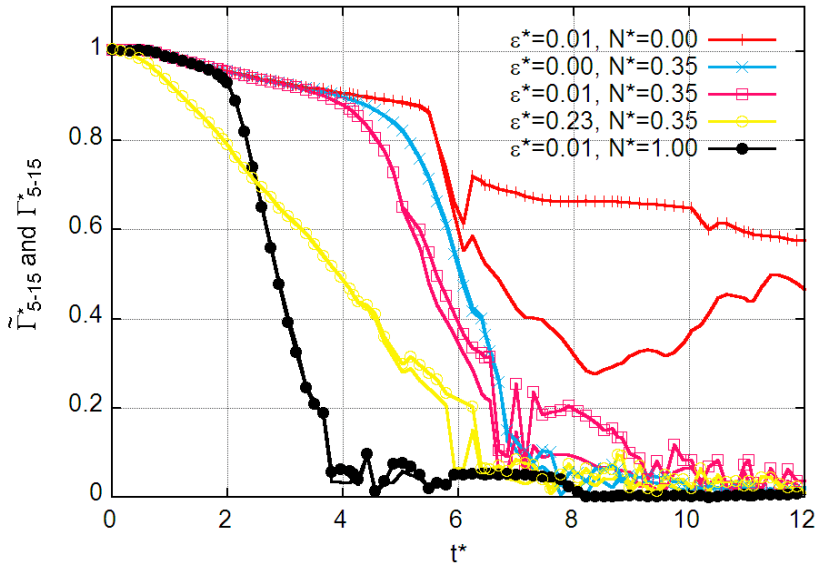

Figure 3. Circulation evolutions of MGLET simulations for different degrees of ambient turbulence and temperature stratification.

Figure 2 and Figure 3 show the temporal evolutions of normalized radii-averaged circulations for the different investigated environmental conditions achieved with LESTUF and MGLET simulations. Solid lines indicate $\Gamma^*_{5\text{-}15}$-values that are determined in planes oriented perpendicular to the flight direction. This approach corresponds to the standard method for the evaluation of numerical simulations and to scanning strategies of field measurements of wake vortices with lidar.

We have developed a post processing method that is capable to identify the vortices even in progressed states of vortex decay where the coherent vortex structure is getting lost[7]. For this purpose the method first determines the orientation of a local vortex segment based on the vorticity vector. The next vortex line position found along the direction of the vorticity vector is corrected by a center-of-gravity method based on the pressure minimum. The pressure minimum turned out to be a very robust criterion for the determination of the vortex center position because it results from an integration of the centrifugal forces of the surrounding, also incoherently rotating fluid elements. In Figure 2 and Figure 3 circulation values determined perpendicular to the identified local vortex segments, $\tilde{\Gamma}^*_{5\text{–}15}$, are denoted by symbols.

In contrast to the well established two-phase circulation decay characteristics (solid lines), the vortex circulation estimated perpendicular to the deformed vortex core lines (lines with symbols) reveals a three-phase decay sequence in weakly or neutrally stratified conditions (see Figure 2 and Figure 3). The initial phase of gradual decay termed “diffusion phase” is followed by a “rapid decay phase” which typically commences shortly before the vortices link. The circulation decrease during the short rapid decay phase is caused by the mutual annihilation of vorticity in the linking area. Subsequently, in neutrally stratified environments long-living vortex rings are observed with gradual vortex decay. This third phase may be termed “ring diffusion phase”. The small axial extension of the vortex ring (cf. Figure 6 at the normalized vortex age of t* = 8.1) may explain why conventional data evaluation procedures, that evaluate circulation only in planes oriented perpendicular to the flight direction, may estimate erroneously that the vortex has rapidly decayed to small circulation values.

The differences between the circulation evolutions achieved by the two different codes are relatively small in the stably stratified cases. However, in the neutrally stratified case the differences are considerable. Substantial uncertainties in neutrally stratified cases are also reported in other numerical studies and experiments. In stably stratified environments the baroclinic vorticity generated around the vortex oval appears to be a robust phenomenon controlling the wake vortex behavior[8]. On the other hand, in neutrally stratified environments peculiarities of the turbulence fields appear to have a strong impact on maximum vortex lifetimes and descent distances. Numerical

simulations[9] demonstrate that even simple displacements of the initial wake vortex positions in a statistically identical background turbulence field may substantially shift the time of vortex linking and subsequent decay. The authors state that the sensitivity to local turbulence topology may be explained by the excitation of different modes of vortex distortion due to locally different spectral power of the atmospheric turbulence.

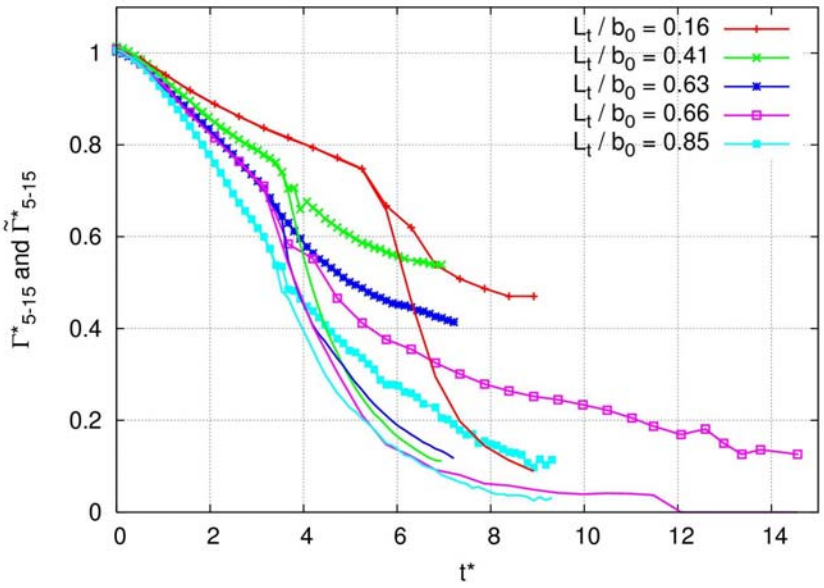

Figure 4. Circulation evolutions of LESTUF simulations for different integral turbulence length scales, L_t ($\varepsilon^* = 0.23$, $N^* = 0$).

Results of a simulation series with $\varepsilon^* = 0.23$ and $N^* = 0$ and varying integral turbulent length, L_t, scales are shown in Figure 4. Except for $L_t/b_0 = 0.16$ the onset of rapid decay occurs at similar instants of time, but the corresponding circulation evolution differs strongly already in the diffusion phase. With increasing L_t/b_0 the circulation decay in the diffusion phase speeds up and, as a consequence, the three-phase decay is more and more concealed.

Figure 5 indicates that with increasing L_t/b_0 the amount of the generated secondary vorticity structures is significantly increased during the diffusion phase. In neutrally stratified cases secondary vorticity is exclusively generated by tilting and stretching of the surrounding turbulent eddies. During the stretching process the primary vortices perform work on the secondary vortices whereby the primary vortices, in turn, lose rotational energy as delineated in Ref. 10. Note that for constant eddy dissipation rates increased integral turbulence length scales correspond to more energetic turbulence fields. This suggests that the intensity of environmental turbulent kinetic energy impacts circulation decay in the diffusion phase and may conceal the two-phase and three-phase decay characteristics.

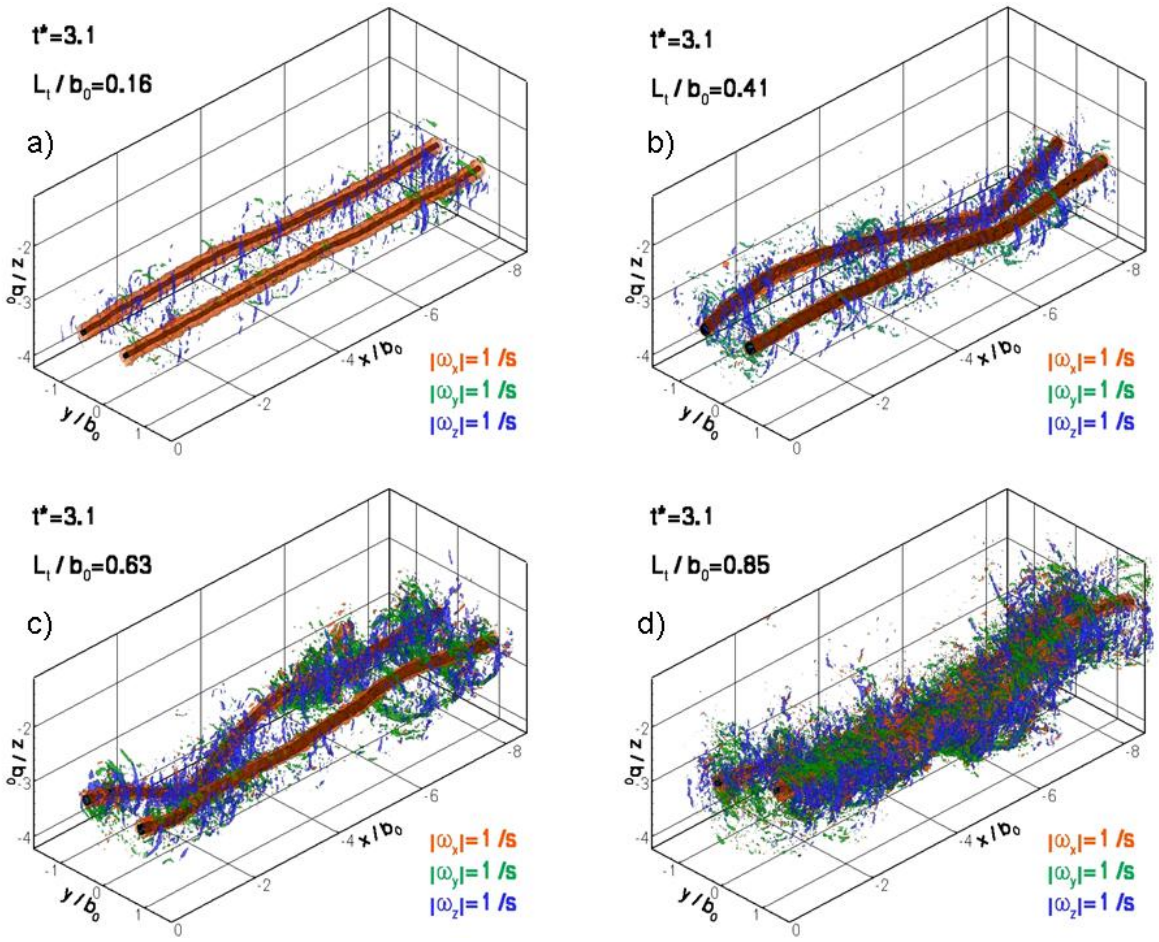

Figure 5. Vortex topology and secondary vorticity for different integral turbulence length scales at t^*=3.1 (ε^* = 0.23, N^* = 0, LESTUF).

For integral length scales exceeding one initial vortex spacing the influence of L_t should be negligible as a parameter for vortex decay characterization[11]. However, if $L_t/b_0 < 1$ it should be considered together with ε^* to characterize vortex decay driven by atmospheric turbulence. For example, in the atmospheric surface layer L_t depends on the distance to the ground and can reach small values in ground proximity. In field experiments it has been observed that wake vortex decay in ground proximity is only very weakly dependent on the eddy dissipation rate[12, 13]. The described sensitivity on L_t/b_0 suggests that this may be related to the reduced turbulence length scales in the surface layer. Consequently, vortex decay mechanisms at the ground are mainly controlled by the interaction of the wake vortices with the secondary vortices detaching from the boundary layer[12].

We suppose that the good agreement between simulated decay rates and decay rates measured by lidar in the diffusion phase achieved with older numerical simulations are related to diffusive subgrid scale models or numerical schemes leading to overestimated vortex core growth rates. Only with increasing computational performance and advanced numerical schemes and subgrid scale closures it has become feasible to allow for the simulation of compact vortex cores in sufficiently large simulation domains allowing for large integral turbulence length scales.

IV. Vortex Topology

The evolution of the vortex topology from the initial sinusoidal oscillations, the subsequent vortex linking and vortex ring formation up to the axial contraction and the lateral spreading of the vortex ring (see Figure 6) can be explained phenomenologically by mutual velocity induction. For example, at $t^* = 5.9$ the lower ends of the vortex rings do not only mutually induce a vertical descent speed but due to their partially vertical orientation also induce a propagation velocity in flight direction leading to an axial compression of the vortex rings. Similarly, the upwards bended vortex pairs at $t^* = 8.1$ cause a sustained widening of the vortex rings.

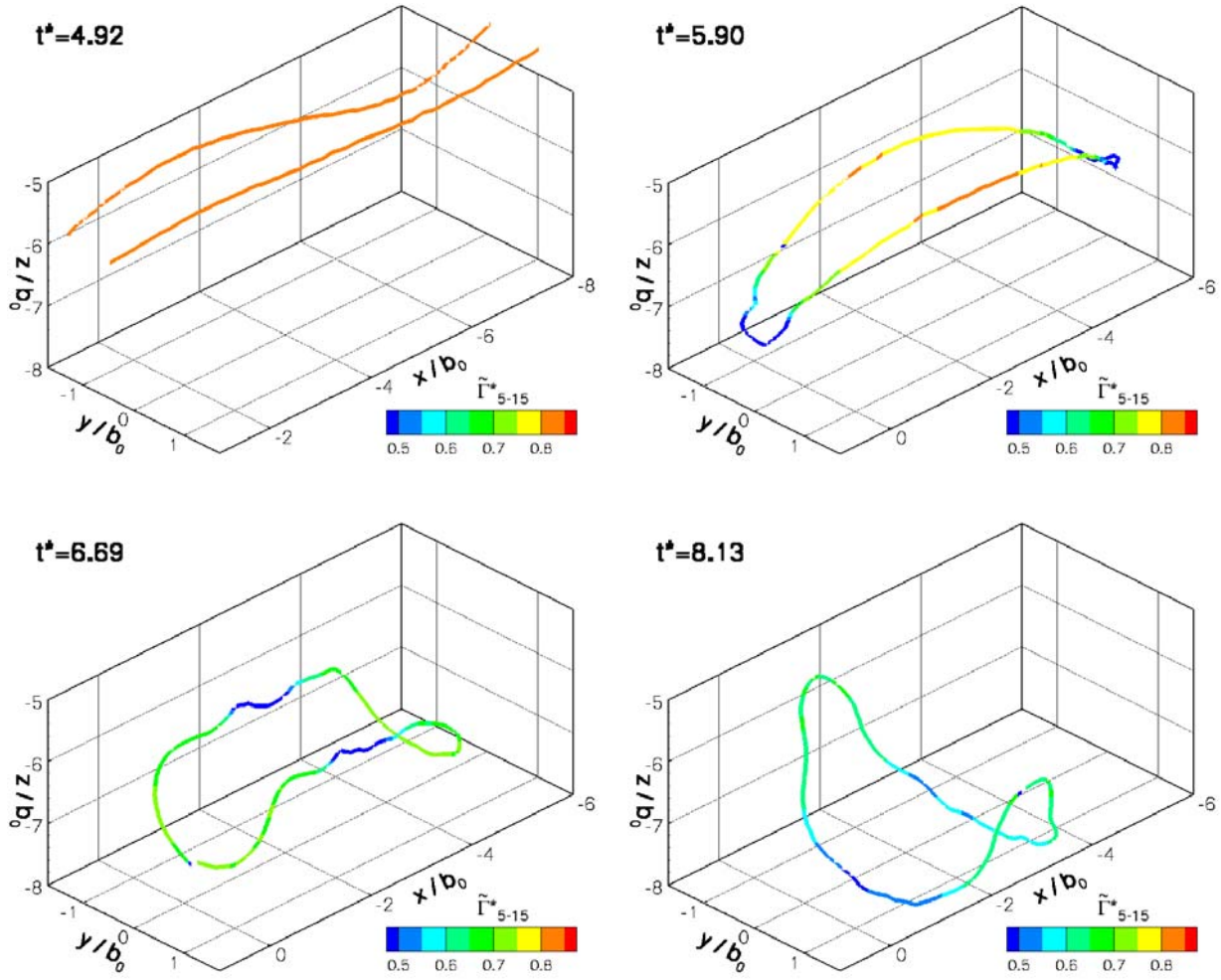

Figure 6. Temporal evolution of wake vortex topology with color-coded circulation in a neutrally stratified environment with weak to moderate turbulence (ε* = 0.05, L_t/b_0 = 0.41, LESTUF).

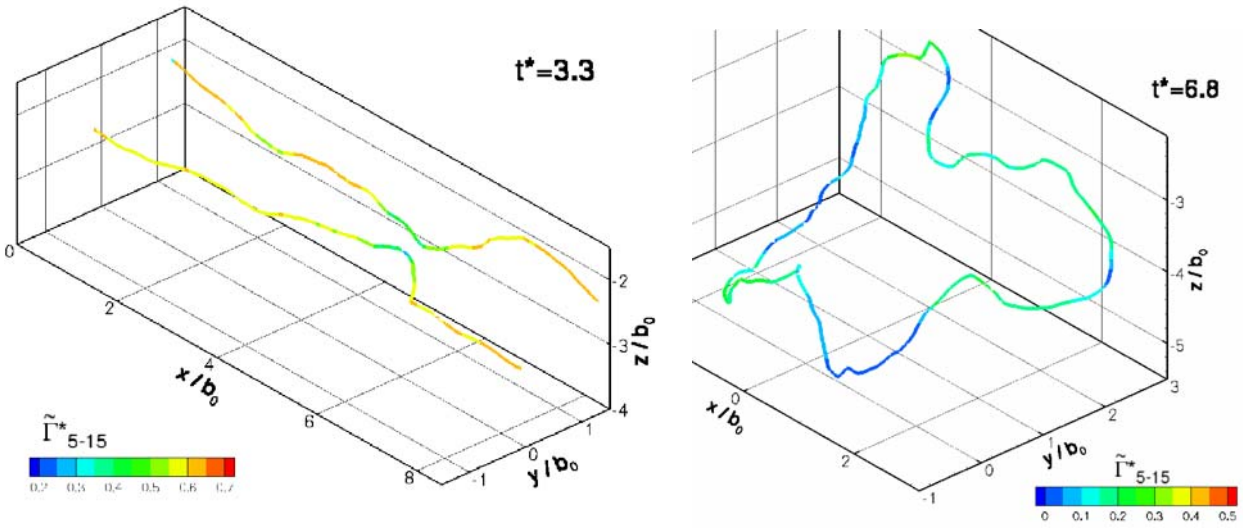

Figure 7. Complex vortex ring topology with color-coded circulation in a neutrally stratified environment with moderate to strong turbulence ($\varepsilon^* = 0.23$, $L_\ell/b_0 = 0.85$, LESTUF).

A comparison of Figure 6 and Figure 7 indicates that with increasing turbulence intensity and increasing turbulence integral length scales the vortex topology is becoming more complex and the classical shape of the Crow instability and the ring formation is getting lost in favor of superimposed random deformations caused by large scale turbulent eddies.

Another interesting aspect illustrated in Figure 6 is the shifting of the local minimum of radii-averaged circulation, $\tilde{\Gamma}^*_{5-15}$, from the linking area at $t^* = 5.9$ to the transverse side at $t^* = 6.7$ and back to the former linking area at $t^* = 8.1$. This shifting process goes along with a variation of the vortex core radii where large radii correspond to small $\tilde{\Gamma}^*_{5-15}$ values. It can be explained by stretching and compression of the respective vortex segments again caused by mutual velocity induction and, complementarily, by the propagation of pressure waves along the vortex tubes that increase core radii when the waves collide (vortex bursting)[14]

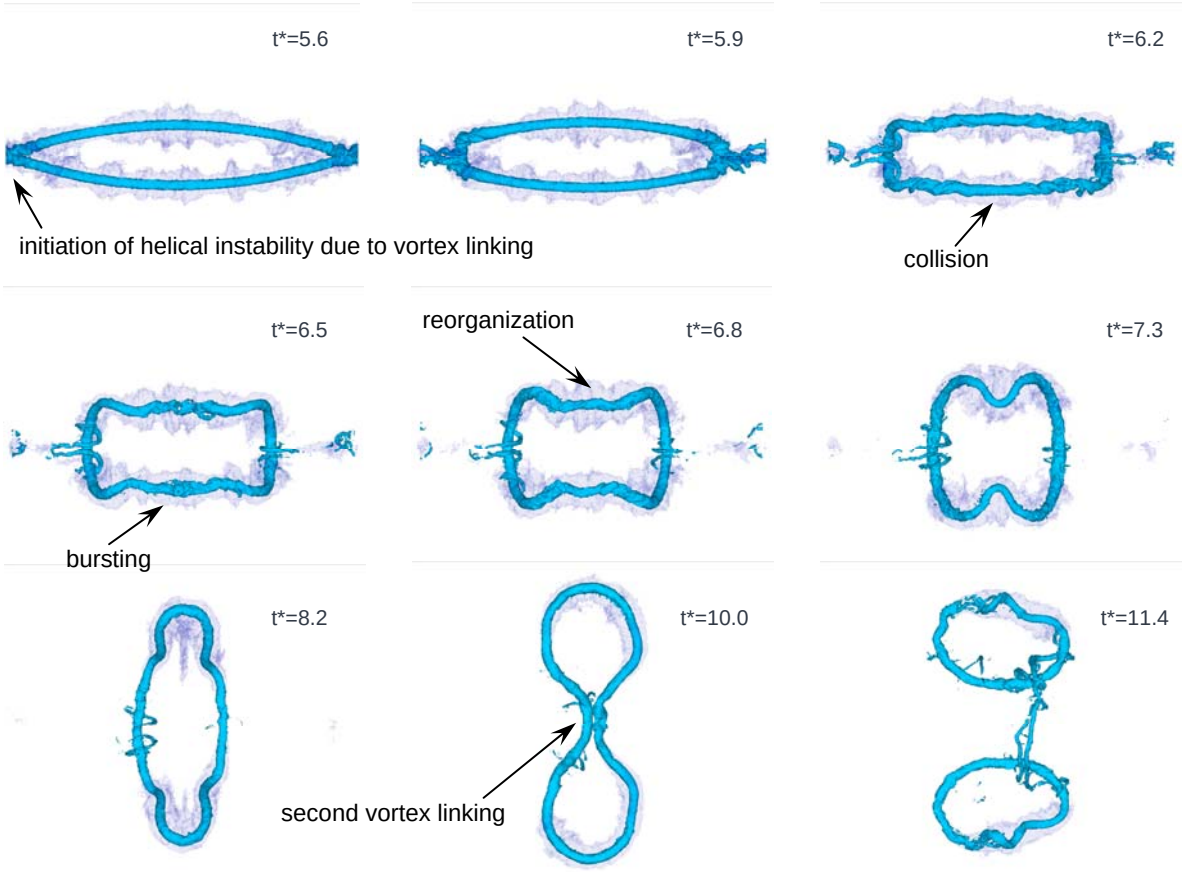

Figure 8. Isosurfaces of vorticity magnitude ($|\omega| = 1.5\ s^{-1}$) and of passive tracer distribution (25% of tracer concentration initialized in vortex cores) indicating the formation of helical instabilities traveling along the vortices ($\varepsilon^* = 0.01$, $N^* = 0$, $L_t/b_0 = 0.85$, MGLET).

Figure 8 indicates that during vortex reconnection pressure disturbances are generated that subsequently are traveling as pressure waves along the vortices and are visualized in terms of helical instabilities[14]. At $t^* = 6.2$ the waves collide leading to a temporal local increase of core radii and a corresponding decrease of $\widetilde{\Gamma}^*_{5-15}$ followed by a reorganization of the vortex structure and of $\widetilde{\Gamma}^*_{5-15}$ values (cf. Figure 6). The pressure waves continue to propagate along the vortices and collide another time in the former reconnection area. Ref. 14 argues whether the vortex collision might lead to the vortex bursting phenomenon described by Spalart[15]. However, the tracer distributions in Figure 8 do not indicate lateral spreading of the passive tracer associated with vortex bursting. In section V. we suggest an alternative explanation for the vortex bursting phenomenon observed during smoke visualizations or at contrails. The formation of helical instabilities is still observed in weakly stably stratified conditions ($\varepsilon^* = 0.01$, $N^* = 0.35$) but the interaction of the helical instabilities with the baroclinic vorticity prevents the reorganization of the vortex ring.

Further, Figure 8 delineates that after $t^* = 10$ the vortex ring transforms into a double ring. The unusual recovery of Γ^*_{5-15} after $t^* = 8$ of case ($\varepsilon^* = 0.01$, $N^* = 0$) in Figure 3 is related to an increase of the ring segment length oriented in flight direction and a redistribution of circulation along the vortex rings. Note that the typical structures of the bridging process also appear during the formation of the double ring. The author once could personally observe the formation of double rings visualized by contrails.

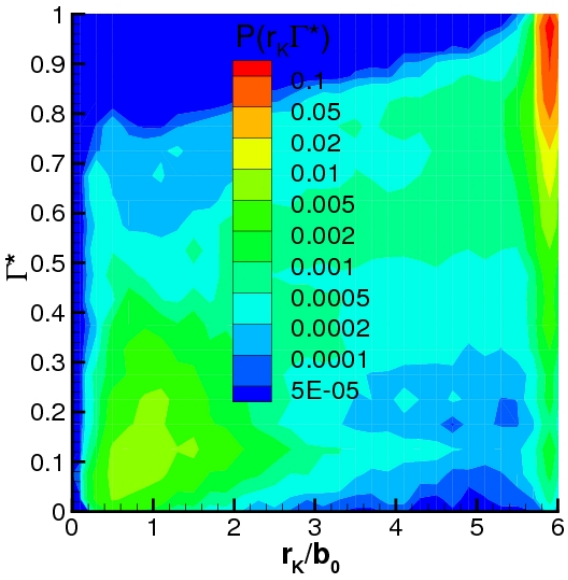

Figure 9. Joint probability density distribution of curvature radii and circulation averaged for the nine parameter combinations of ε^* and N^* of the LESTUF simulations.

For segments of the deformed vortex core lines with lengths of 1.5 initial vortex spacings, b_0, we characterize the vortex deformation in terms of curvature radii[7]. Despite the wide range of meteorological conditions and the resulting vortex lifetimes and varying decay characteristics, the statistics of vortex curvature radii look quite similar for all the conducted LES with LESTUF (see table 1). An inspection of the investigated cases reveals that the development of the curvature radii distributions is well correlated with circulation decay. Figure 9 displays joint probability density distributions (JPDDs) of curvature radii dependent on normalized circulation which have been established from the post-processing of the nine LES.

Because the method to derive curvature radii, r_κ, employs a maximum of $r_\kappa/b_0 = 6$, vortex segments with $r_\kappa/b_0 > 5$ are considered to be straight in principle. Curvature radii r_κ are completely larger than $5b_0$ only for $\Gamma^*_{5\text{-}15} > 0.95$. Already at $\Gamma^*_{5\text{-}15} = 0.8$ curvature radii below $r_\kappa/b_0 = 1$ show up. At $\Gamma^*_{5\text{-}15} \approx 0.6$ about 50% are still straight. At a late stage of vortex evolution the established statistics indicate a predominance of curvature radii on the order of one initial vortex separation, b_0. It still has to be investigated thoroughly whether such strongly deformed vortex segments may still pose a risk to follower aircraft. For this purpose idealized vortex flow fields and LES data are being applied within flight simulator tests[16]. Encounter flights of the DLR research aircraft Falcon behind an A380 indicate that already pronounced sinusoidal oscillations prior to vortex linking might significantly reduce the severity of encounters.

V. Turbulent Exchange Processes of Passive Tracer

The investigation of turbulent exchange processes of passive tracers within the descending vortex oval and between the oval and its environment is of interest with respect to several aspects: (i) The dispersion of the ice crystals during the vortex descent is an important parameter in order to quantify the vertical extent, optical thickness, and lifetime of the contrails produced during cruise. Currently, it is not yet clear how strong the contribution of contrails to global warming might be[17]. (ii) For inviscid point vortices the circulation can only decay as a result of diffusion of vorticity across the centerline between the vortices[18]. So the exchange processes between the passive tracers may be indicative of the annihilation of the counter-signed vorticity. (iii) The simultaneous investigation of the topology of the tracer distribution and the vortex dynamics may indicate to which extent visual observations of contrails or vortices visualized by smoke actually represent the dynamical vortex evolution.

A nice example of a misleading tracer footprint is shown in Figure 10 for the reference cruise conditions case. After linking the vortex ring rapidly contracts leaving behind a tracer structure pretending an active vortex pair.

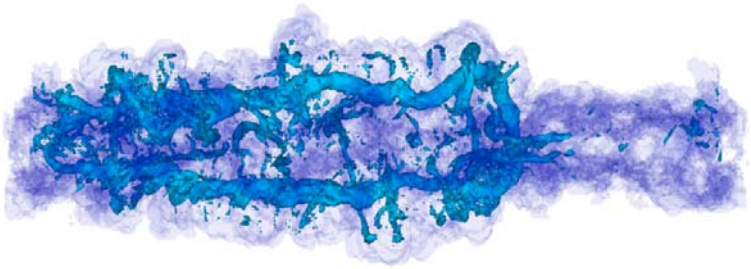

Figure 10. Topview of isosurfaces of vorticity magnitude ($|\omega| = 1.5\ s^{-1}$) and of passive tracer distribution (5% of tracer concentration initialized in half oval) at $t^* = 5.9$ ($\varepsilon^* = 0.01$, $N^* = 0.35$, $L_t/b_0 = 0.95$, MGLET).

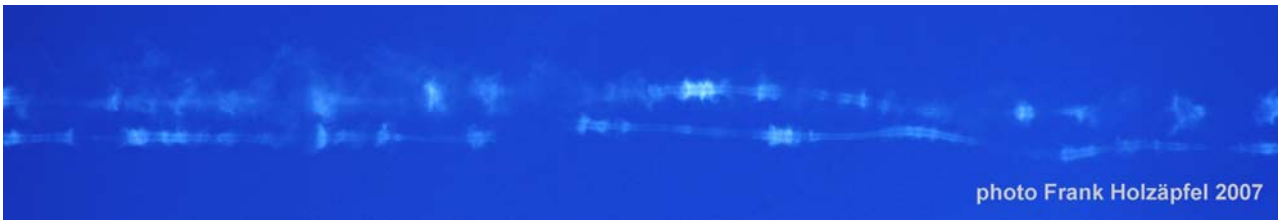

Figure 11. Photograph of a contrail generated by a two-engine commercial jet airplane indicating ice crystal redistribution along vortex lines.

Figure 11 displays a photograph of a contrail generated by a two-engine commercial jet airplane. The vortex cores appear hollow indicating reduced ice crystal concentrations within the cores. This may be explained either by reduced turbulent mixing of the jet exhaust into the vortex cores caused by their centrifugal stability[2]. Alternatively, the ice particles may be centrifuged out of the core by the centrifugal forces of the strongly rotating cores. Third, it could be attributed to warm jet exhaust gases accumulating inside the centrifugally stable vortex core driven by buoyancy effects and causing local subsaturation with respect to ice crystals. Possibly, a combination of more than one of these effects is responsible for the generation of the hollow vortex tubes.

Another prominent feature of Figure 11 is the pronounced axial redistribution of ice crystals along the vortex tubes, a phenomenon termed vortex bursting, puffs or pancake vortices[15]: The region marked by ice crystals contracts in portions of the vortices and expands in others.

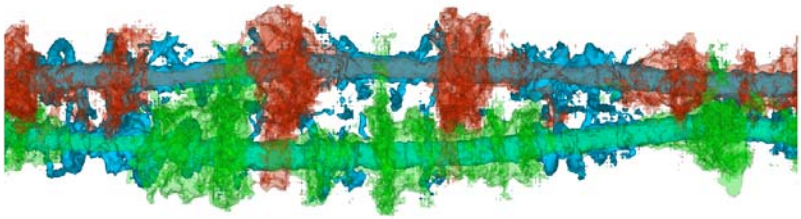

Figure 12. Topview of isosurfaces of vorticity magnitude ($|\omega| = 1.2\ s^{-1}$, blue) and of passive tracer distributions (25% of tracer concentration initialized in half oval, red and green) at $t^* = 4.6$ ($\varepsilon^* = 0.01$, $N^* = 0.35$, $L_t/b_0 = 0.95$, MGLET).

The MGLET simulations of the reference case for cruise conditions ($\varepsilon^* = 0.01$, $N^* = 0.35$) exhibit a comparable tracer topology (see Figure 12, red and green). For this qualitative comparison a similar phase of vortex evolution prior to vortex linking ($t^* = 4.6$) has been chosen as depicted in the photograph in Figure 11. Clearly, the tracer is being pushed along the vortex tubes and accumulates in distinct areas where it spreads out indicating the vortex bursting phenomenon. At some locations the tracer has started to pass over to its neighboring vortex. In between the tracer accumulations, the tracer is restricted to the vortex core regions. Figure 13 indicates that for increased turbulence intensity ($\varepsilon^* = 0.23$, $N^* = 0.35$) the redistribution process is even more pronounced: More significant accumulations of the passive tracers at less axial positions occur at earlier times ($t^* = 2.3$).

A more detailed analysis (see below) indicates that the secondary vortex structures (SVS) formed by simultaneous stretching and tilting of baroclinic vorticity and of turbulent eddies[10] drive the axial redistribution process. Figure 12 and Figure 13 feature rip-shaped and helical SVS (blue) that induce themselves a propagation velocity[10] and thus push the tracer along the vortex tubes. Behind the SVS the tracer remains in the core region whereas the puffs are produced by approaching and colliding SVS.

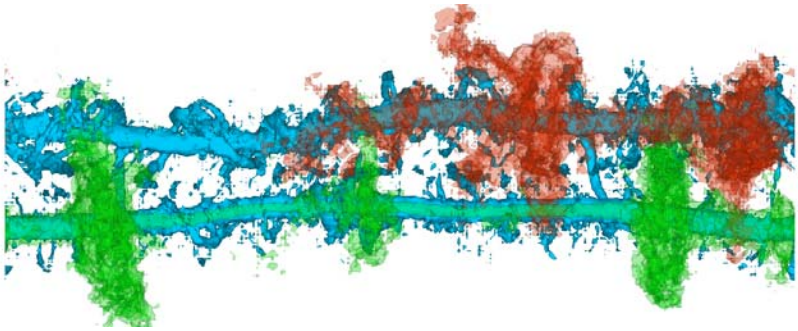

Figure 13. Topview of iso-surfaces of vorticity magnitude ($|\omega| = 1.2$ s^{-1}, blue) and of passive tracer distributions (25% of tracer concentration initialized in half oval, red and green) at $t^* = 2.3$ ($\varepsilon^* = 0.23$, $N^* = 0.35$, $L_t/b_0 = 0.75$, MGLET).

Figure 14 shows quantities evaluated in ring segments extending within radii from 15 m to 25 m around the centerline of the upper vortex depicted in Figure 12 ($\varepsilon^* = 0.01$, $N^* = 0.35$). Figure 14 top left shows the azimuthal vorticity in these ring segments as it develops during the vortex descent. SVS pairings can be identified that approach each other while they are gaining strength. For example, one SVS originates from ($x = 120$ m, $z = 340$ m) while its counter-rotating mate is generated at ($x = 180$ m, $z = 340$ m). At ($x = 150$ m, $z = 270$ m) the SVS collide. The SVS go along with axial transport velocities (Figure 14, top right) generating the respective tracer accumulation and thinning seen in the lower left part of the figure. The V-shaped tracer accumulations indicate how two counter-rotating SVS push the tracer ahead until the collision and spreading of the tracer occurs. The $\Gamma^*_{5\text{-}15}$-evolution in Figure 14 bottom right clearly indicates that the tracer redistribution does not influence the local vortex strength. So although the visual appearance of vortex bursting may suggest local vortex weakening it is not associated with local vortex decay or the vortex breakdown phenomenon.

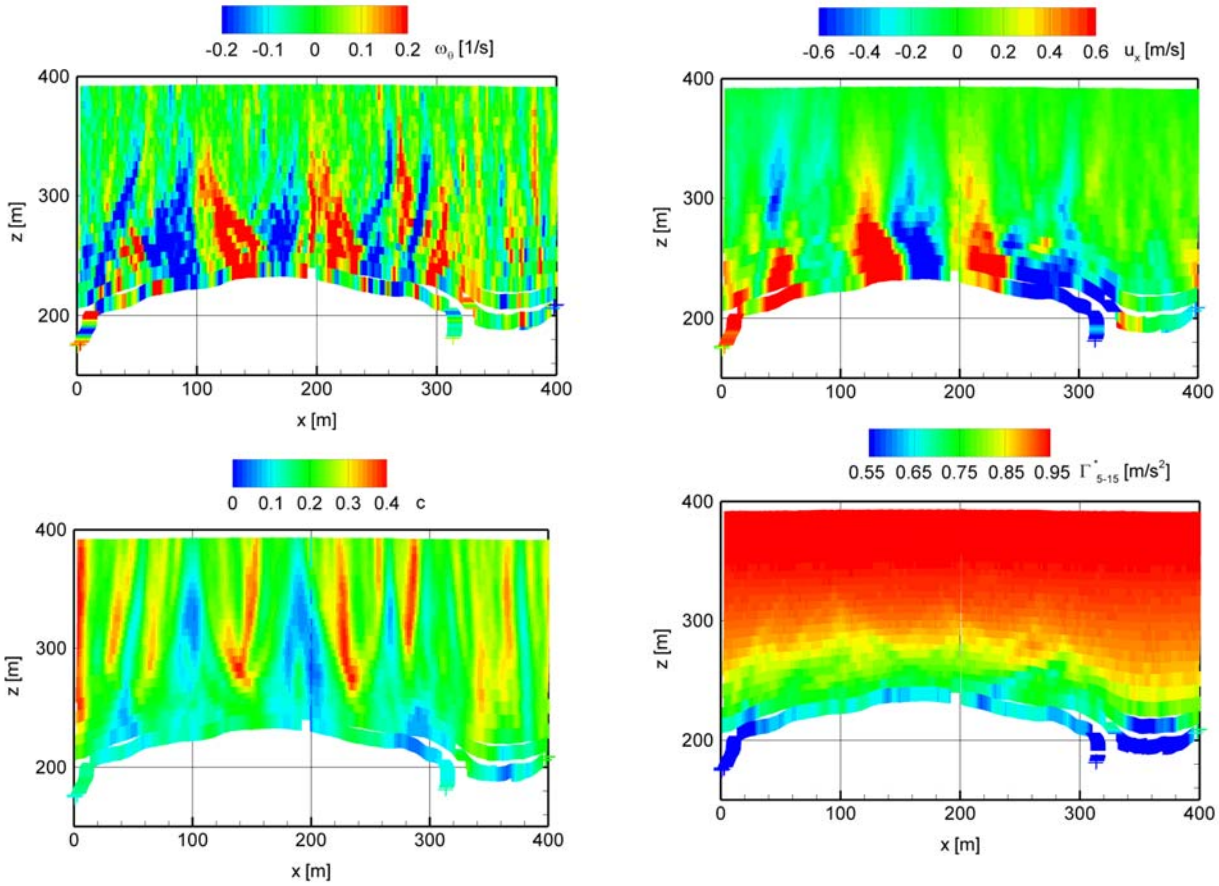

Figure 14. Azimuthal vorticity (top left), axial velocity (top right), tracer concentration (bottom left) evaluated within radii from 15 m to 25 m around centerline of upper vortex depicted in Figure 12. Right below normalized circulation. All quantities plotted against vertical vortex position. ($\varepsilon^* = 0.01$, $N^* = 0.35$, $L_t/b_0 = 0.95$, MGLET).

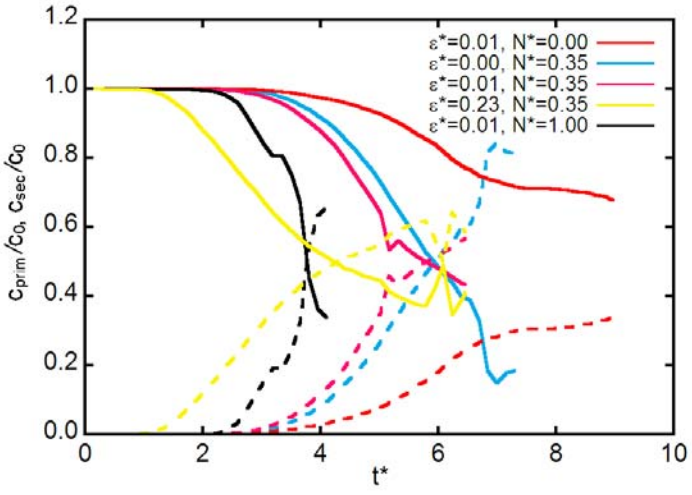

Figure 15. Temporal evolutions of tracer concentrations in primary (solid lines) and secondary wakes (dashed lines). Tracer initialized in half oval (MGLET).

Figure 15 illustrates the detrainment of the passive tracer from the primary wake (solid lines) and the corresponding tracer concentration increase in the secondary wake (dashed lines). The tracer is attributed to the primary wake when it resides within a cylindrical volume with a radius of b_0 centered on the identified vortex tracks. This method allows distinguishing between primary and secondary wake also for extensively deformed vortices and during the vortex-ring regime. Figure 15 shows results of the simulations where the tracer initially covered 50% of the oval cross-section.

The vortex detrainment characteristics feature striking similarities with the circulation decay characteristics (see Figure 3). The sequence of the different cases with respect to the onset of rapid circulation decay and the onset of detrainment is the same. The times when the circulation has reached 50% of its initial value approximately coincide with the times when 50% of the tracer has been detrained. However, in several cases the primary wake may still contain approximately 40% of its initial tracer concentration when the wake has already fully decayed.

The detrainment characteristics of the three different tracer initializations are similar (not shown). For the initialization in the full oval the detrainment starts almost immediately whereas it is delayed for the half oval and slightly further delayed for the tracer initialization within the vortex cores. A similar time shift is observed for the instant when 50% of the tracer is detrained. The tracer initializations within the full oval and the vortex core can be considered as extreme limits embracing realistic scenarios. As a consequence, the similar characteristics of the detrainment rates of the three different initializations indicate a relatively low sensitivity of detrainment rates on initial tracer distributions within the wake.

VI. Conclusion

Large eddy simulations of wake vortex evolution in various turbulent and stably stratified atmospheric environments have been conducted with two different LES codes. Passive tracers are used to investigate exchange processes between the vortex cores, the vortex oval and its environment as well as redistribution processes along the vortex tubes. A post processing method is used to identify the vortex center lines even in progressed states of vortex decay where the coherent vortex structure is getting lost. This method allows, for example, analyzing the circulation evolution of vortex rings and revealing the mechanisms of the vortex bursting phenomenon.

In contrast to the well established two-phase circulation decay characteristics, the vortex circulation estimated perpendicular to the deformed vortex core lines reveals a three-phase circulation decay sequence in weakly or neutrally stratified conditions. The initial phase of gradual decay termed “diffusion phase” is followed by a “rapid decay phase” which typically commences shortly before the vortices link. In the subsequent “ring diffusion phase” long-living vortex rings are observed with gradual vortex decay in neutrally stratified environments. It may be argued that the typical weak stable temperature stratification prevailing at cruise altitudes may prevent wake vortices from excessive descent distances reaching beyond adjacent flight levels.

We find that variations of integral turbulence length scales, $L_{t,}$ of the atmospheric turbulence may strongly impact vortex decay characteristics for given eddy dissipation rates, ε. With increasing turbulence length scales the circulation decay in the diffusion phase speeds up and, as a consequence, the three-phase decay is more and more concealed. The responsible mechanism corresponds to the classical concept of turbulence theory stating that the energy transfer from large eddies (wake vortices) to smaller eddies (environmental turbulent flow or baroclinic vorticity) is related to the work conducted by the large eddies by stretching of the smaller eddies. It appears that the amount of environmental vorticity (turbulent eddies) controls the circulation decay in the diffusion phase. It can be anticipated that for sufficiently large turbulence length scales ($L_t/b_0 > 1$) the effect of turbulence can be fully parameterized solely based on eddy dissipation rates. Conversely, this means that for $L_t/b_0 < 1$ (for example in ground proximity) the effect of eddy dissipation is reduced and both parameters L_t and ε are necessary to parameterize vortex decay.

The evolution of the vortex topology from the initial sinusoidal deflection, the subsequent vortex linking and vortex ring formation up to the axial contraction and the lateral spreading of the vortex ring can be explained phenomenologically by mutual velocity induction. Vortex deformation is characterized in terms of curvature radii statistics. The development of the curvature radii distributions appears to be well correlated with circulation decay. At a late stage of vortex evolution a predominance of curvature radii on the order of one initial vortex separation, b_0, is found. The alleviation of wake vortex encounters coming along with vortex deformation and the respective decreased impact times of adverse moments and forces is subject of ongoing investigations.

Stretching and compression of vortex segments by mutual velocity induction and, complementarily, by the propagation of pressure waves along the vortex tubes modify vortex core radii and thus radii-averaged circulation.

Pressure waves generated during vortex linking become manifest in helical instabilities. Colliding pressure waves cause a temporary and local decrease of radii-averaged circulation followed by a recovery. During this collision spreading of the tracer attributed to the vortex bursting phenomenon is not observed.

Pronounced axial redistribution of the tracer and the so-called vortex bursting phenomenon (formation of puffs or pancake vortices) is observed prior to vortex linking. It is revealed that the mechanism of vortex bursting is related to secondary vorticity structures generated from environmental turbulence or baroclinic vorticity. These ring-shaped or helical vortex structures propagate along the vortex lines thus accumulating the passive tracer ahead. Colliding secondary vortex structures lead to abrupt spreading of the tracer and thus provoke vortex bursting as it can be observed visualized by smoke or contrails.

The detrainment of passive tracer from the primary wake progresses similar as the circulation evolution. For example, the half-life periods of the tracer concentration in the primary wake and the circulation are quite close. Subsequently, the detrainment rates are reduced such that the primary wake may still contain approximately 40% of its initial tracer concentration when the wake has fully decayed. The sensitivity of detrainment rates on particular initial tracer distributions within the wake appears low.

Acknowledgments

The provision of the LES code MGLET and the kind support during its modifications by Florian Schwertfirm of Kreuzinger + Manhart Turbulenz GmbH and by Michael Manhart of Technische Universität München is greatly acknowledged. The supply of computation time on the supercomputers IBM p575 system at Deutsches Klimarechenzentrum (DKRZ) and of SGI Altix 4700 system at Leibniz-Rechenzentrum (LRZ) is greatly appreciated. The current work has been conducted within the DLR project Wetter & Fliegen (Weather & Flying).

References

[1]Kaltenbach, H.-J., Gerz, T., and Schumann, U., "Large-eddy simulation of homogeneous turbulence and diffusion in stably stratified shear flow," J*ournal of Fluid Mechanics*, Vol. 280, 1994, pp. 1-40.

[2]Holzäpfel, F., "Adjustment of Subgrid-Scale Parametrizations to Strong Streamline Curvature," *AIAA Journal*, Vol. 42, 2004, pp. 1369-1377.

[3]Manhart, M., "A Zonal Grid Algorithm for DNS of Turbulent Boundary Layers," *Computer & Fluids*, Vol.33, 2001, pp. 435-461.

[4]Hokpunna, A., and Manhart, M., "Compact Fourth-order finite volume method for numerical solutions of Navier-Stokes Equations on Staggered grids," *Journal of Computational Physics*, accepted for publ. 2010, doi: 10.1016/j.jcp.2010.05.042.

[5]Meneveau, C., Lund, T. S. and Cabot, W. H., "A Lagrangian Dynamic Subgrid-scale Model of Turbulence," *Journal of Fluid Mechanics*, Vol. 319, 1996, pp. 353–385.

[6]Schumann U., Konopka P., Baumann R., Busen R., Gerz T., Schlager H., Schulte P., and Volkert H., "Estimates of diffusion parameters of aircraft exhaust plumes near the tropopause from nitric oxide and turbulence measurements," *Journal of Geophysical Research*, Vol. 100, No. D20, 1995, pp. 14147-14162.

[7]Hennemann, I., and Holzäpfel, F., "Aircraft Wake Vortex Curvature and Resulting Risk Potential for Following Aircraft," *CEAS 2009 European Air and Space Conference*, Manchester, UK, 2009, 9 pages.

[8]Holzäpfel F., Gerz, T., and Baumann R., "The turbulent decay of trailing vortex pairs in stably stratified environments," *Aerospace Science and Technology*, Vol. 5, No. 2, 2001, pp. 95-108.

[9]Gerz, T., Baumann, R., "Decay characteristics of single and double wake-vortex pairs in different atmospheric flow realisations", *ICAS 2006, 25th International Congress of the Aeronautical Sciences*, Hamburg, ICAS 2006-3.8.1., Sept. 2006, pp. 13.

[10]Holzäpfel, F., Hofbauer, T., Darracq, D., Moet, H., Garnier, F., Ferreira Gago, C., "Analysis of wake vortex decay mechanisms in the atmosphere," *Aerospace Science and Technology*, Vol. 7, 2003, pp. 263-275.

[11]Crow, S. C., and Bate, E. R., "Lifespan of Trailing Vortices in a Turbulent Atmosphere," *Journal of Aircraft*, Vol. 13, No. 7, 1976, pp. 476-482.

[12]Holzäpfel, F., and Steen, M., "Aircraft Wake-Vortex Evolution in Ground Proximity: Analysis and Parameterization, *AIAA Journal*, Vol. 45, No. 1, 2007, pp. 218-227.

[13]Burnham, D. C., and Hallock, J. N., "Measurements of Wake Vortices Interacting with the Ground, AIAA Paper 98-0593, 1998.

[14]Moet, H., Laporte, F, Chevalier, G., and Poinsot, T., "Wave propagation in vortices and vortex bursting," *Physics of Fluids*, Vol. 17, 2005, pp. 054109-1 - 054109-15.

[15]Spalart, P. R., "Airplane Trailing Vortices," *Annual Review of Fluid Mechanics*, Vol. 30, 1998, pp. 107-138.

[16]Vechtel, D., "Curved wake vortices encounter simulations with pilots-in-the-loop," WakeNet3-Europe Workshop, Berlin, http://wakenet3-europe.org/fileadmin/user_upload/SpecificWorkshop_WV_EncounterSimulation/1st_day/Dennis_Vechtel.pdf, 2010.

[17]Schumann, U., "A contrail cirrus prediction tool," *Intern. Conf. on Transport, Atmosphere and Climate*, DLR/EUR, www.dlr.de/pa/desktopdefault.aspx/tabid-2559/3824_read-19960, Aachen and Maastricht, 2009.

[18]Donaldson, C. d., and Bilanin, A. J., "Vortex Wakes of Conventional Aircraft", NATO, AGARD-AG-204., 1975.